ADVANCED MATERIALS
www.advmat.de

Coexistence of Both Localized Electronic States and Electron Gas at Rutile TiO_2 Surfaces

Shengchun Shen, Meng Wang, Yang Zhang, Yingjie Lyu, Di Tian, Chang Gao, Youwen Long, Jin Zhao, and Pu Yu**

Localized electron polarons formed through the coupling of excess electrons and ionic vibrations play a key role in the functionalities of materials. However, the mechanism of the coexistence of delocalized electrons and localized polarons remains underexplored. Here, the discovery of high-mobility 2D electron gas at the rutile TiO_2 surfaces through argon ion irradiation induced oxygen vacancies is reported. Strikingly, the electron gas forms localized electronic states at lower temperatures, resulting in an abrupt metal–insulator transition. Moreover, it is found that the low-temperature conductivity in the insulating state is dominated by excess free electrons with a high mobility of $\approx 10^3$ cm^2 V^{-1} s^{-1}, whereas the carrier density is dramatically suppressed with decreasing temperature. Remarkably, it reveals that the application of an electric field can lead to a collapse of the localized states, resulting in a metallic state. These results reveal the strongly correlated/coupled nature between the localized electrons and high-mobility electrons and offer a new pathway to probe and harvest the exotic electron states at the complex oxide surfaces.

1. Introduction

Localized polarons, formed by excess charge carriers and their self-trapping due to coupling with phonons (or local lattice distortion), are a pervasive phenomenon in transition metal oxides,[1–6] which is particularly promoted at the surface or interface due to reduced lattice relaxations. It has crucial implications for fundamental physical and chemical properties and related functionalities, such as high-T_C superconductivity,[7] colossal magnetoresistance,[8] thermoelectricity,[9] surface reactivity,[10] photoemission,[11] resistive switching,[12] etc. Depending on the degree of electron localization, polarons can generally be classified into two types: large and small polarons. Large polaron spreads over several lattice sites, forming a shallow electronic state (about 10 meV below the Fermi level) with more free-carrier-like behavior and exhibiting metallic-like transport characteristics. In contrast, a small polaron is usually confined with a range on the order of the lattice constant, which forms a narrow localized in-gap state (about 1 eV below the Fermi level) and shows insulating behavior with slow hopping mobility. Intriguingly, many recent studies have reported that free-like electrons even with high mobility can coexist with small polarons in materials,[13–19] which seems to run counter to the strongly localized nature of small polarons. Furthermore, the underlying mechanism of the coexistence of delocalized electrons and localized polarons remains largely underexplored.

Specifically, rutile TiO_2 is a prototype material to host small polarons due to its unique electron-phonon interaction, which has been heavily investigated by various theoretical and experimental studies.[3,4,20–26] Furthermore, oxygen vacancies can induce 2D electron gas (2DEG) at rutile surfaces,[13,19,27] and therefore rutile TiO_2 forms a promising model system to explore the coupling nature of delocalized electrons and localized polarons.

Here, we utilize argon-ion irradiation to generate oxygen vacancies at the rutile TiO_2 surface and achieve an interesting 2DEG state at the surface (see Experimental Section). The 2DEG shows semiconductive behavior with an abrupt metal–insulator

S. Shen, M. Wang, Y. Zhang, Y. Lyu, D. Tian, P. Yu
State Key Laboratory of Low Dimensional Quantum Physics and Department of Physics
Tsinghua University
Beijing 100084, China
E-mail: scshen@ustc.edu.cn; yupu@mail.tsinghua.edu.cn

S. Shen, C. Gao, J. Zhao
Department of Physics
University of Science and Technology of China
Hefei 230026, China

M. Wang
RIKEN Center for Emergent Matter Science (CEMS)
Wako 351-0198, Japan

Y. Long
Beijing National Laboratory for Condensed Matter Physics
Institute of Physics
Chinese Academy of Sciences
Beijing 100190, China

Y. Long
Songshan Lake Materials Laboratory
Dongguan, Guangdong 523808, China

P. Yu
Frontier Science Center for Quantum Information
Beijing 100084, China

The ORCID identification number(s) for the author(s) of this article can be found under https://doi.org/10.1002/adma.202301453

DOI: 10.1002/adma.202301453

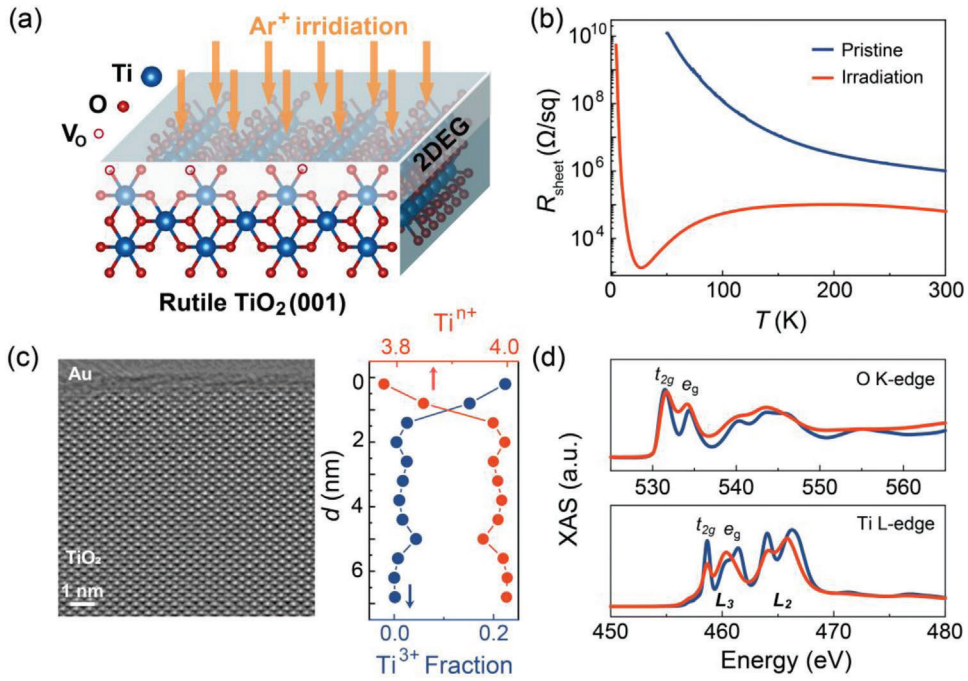

Figure 1. 2D conducting system at the rutile TiO_2 surface induced by oxygen vacancies. a) Schematic diagram of 2DEG at the rutile (001) TiO_2 surface formed by low-energy argon-ion irradiation (V_{Beam} = 300 V, t = 2 min). b) Temperature dependence of sheet resistance for pristine (blue) and irradiated (red) TiO_2 surfaces. c) Atomic crystalline structure of the irradiated TiO_2 surface and corresponding depth dependence of the estimated Ti^{3+} fraction (blue) and Ti average valence (red) extracted from electron energy loss spectra (EELS). d) XAS spectra of the O *K*-edge and Ti *L*-edge for pristine (blue) and irradiated (red) TiO_2 surfaces, measured using the TEY mode.

transition (MIT) at lower temperatures. Interestingly, in contrast to the dramatic increase of sheet resistance by several orders of magnitude in the insulating state, the transporting electron carrier observed by Hall measurement shows a high mobility level of $\approx 10^3$ cm^2 V^{-1} s^{-1}. These results suggest the coexistence of both localized electronic states and high mobility transporting electrons at the reduced TiO_2 surface. Furthermore, we demonstrate that the application of an external electric field can disassociate the localized states into delocalized electrons and consequently introduce a hysteretic-like insulator-to-metal transition.

2. Results and Discussion

2.1. 2DEG at the Rutile TiO_2 Surface

Figure 1a shows a schematic diagram of 2DEG induced by oxygen vacancies at the rutile TiO_2 (001) surface through low-energy argon-ion irradiation. Apparently, the intrinsic surface of rutile TiO_2 is insulating, while it turns into a metallic state after irradiation by argon ions with the introduction of oxygen vacancies (Figure 1b). Strikingly, this metallic surface becomes insulating again at low temperatures, demonstrating an exotic metal-to-insulator (MIT) transition with a transition temperature of ≈30 K. We found that the temperature-dependent sheet resistance ($R_{sheet}(T)$ curves) of irradiated TiO_2 surfaces show similar trends with the observation of an interesting MIT despite the different conditions of argon-ion irradiation employed (Figure S1a, Supporting Information), which suggests a universal transport behavior/mechanism at the low temperature region of the irradiated TiO_2 surface. To obtain direct insight into the spatial confinement of the metallic state at the rutile TiO_2 surface, we further carried out scanning transmission electron microscopy (STEM) measurements on the irradiated samples. Structural analysis shows that argon-ion irradiation leads to the formation of both Ti and O vacancies at the sample surface (Figure 1c). Further atomic-resolved electron energy loss spectra (EELS) studies reveal that the Ti ions at the sample surface are dramatically reduced from Ti^{4+} toward Ti^{3+}, indicating that electron doping is predominantly driven by the formation of oxygen vacancies (Figure 1c; Figure S2, Supporting Information). Moreover, this reduced electron state is strongly confined at the top ≈2 nm of the surface, suggesting the 2D nature of the metallic state. This point was also confirmed by the variation of atomic intensity along the depth direction, obtained from integrated differential phase contrast (iDPC) image analysis (Figure S2c, Supporting Information),[28] in which an obvious decrease in atomic intensity is observed at the surface at ≈2 nm depth. Clearly, the conducting channel induced by ion irradiation is confined into a 2D nature at the surface. Figure 1d shows the X-ray absorption spectroscopy (XAS) spectra of the O *K*-edge and Ti *L*-edge for both the pristine and irradiated TiO_2 surfaces, and here surface sensitive total-electron-yield (TEY) mode was employed. For the O *K*-edge of the rutile TiO_2 surface, the two sharp peaks at approximately 530–535 eV are due to the hybridization between O(2p) and Ti(3d), and peaks located at higher energy are attributed to O(2p)–Ti(2p, 4s, 4p) hybridized states. Compared to the pristine surface, the t_{2g} peak is shifted toward higher energy and its intensity is suppressed for the irradiated surface, and moreover the ratio between t_{2g}/e_g

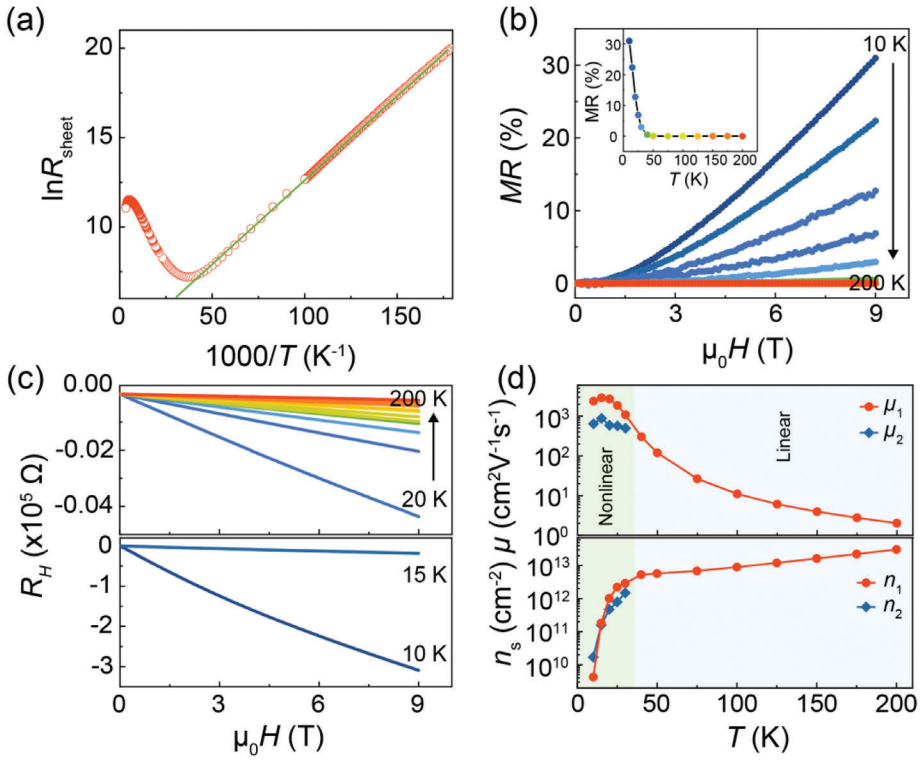

Figure 2. Formation of localized electronic states at the irradiated rutile TiO_2 surface. a) Logarithmic sheet resistance as a function of reciprocal temperature 1000/T for the irradiated TiO_2 surface. The green line is fitted by the thermally activated model at low temperatures. b) Magnetoresistance measurements at different temperatures. The inset shows the temperature dependence of MR at 9 T. c) Magnetic field dependence of the Hall measurements at different temperatures. d) Extracted mobility and carrier density as a function of temperature. The nonlinear Hall resistances at low temperatures were fitted by two channels of electrons (n_1 and n_2).

peak integral area is also notably reduced, and these changes can be attributed to the distortion of TiO_6 crystal symmetry and modification of p–d hybridization states due to the creation of oxygen vacancies.[29–32] The XAS spectra at Ti *L*-edges can provide direct information about the chemical valence state of Ti ions, and the significantly suppressed t_{2g} peaks indicate considerable electron doping into the Ti ions, which could be correlated with the formation of oxygen vacancies. Importantly, the surface sensitive XAS results are quantitively consistent with the atomic resolved EELS data, which points out the intrinsic 2D nature of the formed electronic states. In addition, the irradiated TiO_2 surfaces under different conditions exhibit very similar XAS spectra, which also verifies the universal nature of the formed conducting states through chemical reduction (Figure S1b–e, Supporting Information). Combined with electrical transport, structural and spectral measurements, a 2D conducting surface was resolved at the rutile TiO_2 surface, and moreover our temperature dependent and time dependent measurements prove that such 2DEG shows very robust temporal and thermal stability (Figure S3, Supporting Information).

Previous works reported that, at high polaron density, the repulsive polaron–polaron interaction determines the instability of the lattice structure, which may drive the system into structural reconstruction.[33,34] Along this vein, the surface reconstruction at the TiO_2 surface irradiated with argon ions could be an interesting system to explore the correlation of excess electrons, polarons and structural reconstruction at the conducting surface. For this purpose, we carried out reflection high-energy electron diffraction (RHEED) measurements (Figure S4, Supporting Information) on both pristine and irradiated rutile (001) TiO_2 samples, as the RHEED probes mainly the surface atomic structure due to its small penetration depth. The measurements reveal that the pristine sample shows an atomic smooth surface as evidenced by the clear diffraction spots and streaks. However, all these features disappear for the irradiated sample, suggesting that the atomically flat surface was disordered through argon-ion irradiation. Furthermore, in our study, the effective thickness of the 2DEG is estimated to be ≈2 nm as evidenced by the STEM-EELS analysis, which is one order of magnitude larger than that generally considered for surface reconstruction (monolayer). We note that previous works also demonstrated that the rutile TiO_2 (110) surface irradiated by argon ions exhibits ≈2 nm roughness and a reduced valence state of Ti^{4+}, and importantly it does not show surface reconstruction unless annealed at high temperatures.[35,36] Finally, we note that similar studies on argon irradiated $SrTiO_3$ (111) samples also show the presence of 2DEG with a disordered surface.[37]

2.2. Coexistence of Electron Polarons and High Mobility Electrons

Now, we focus on the MIT at low temperatures. **Figure 2**a shows the Arrhenius plot of the $R_{sheet}(T)$ curves, and the insulating state

below the characteristic temperature (T_M ≈30 K) demonstrates a thermal activation energy of ≈9 meV, which suggests a rather shallow energy for this localized state. Interestingly, the anomalous insulating state shows a relatively large positive magnetoresistance (MR), up to ≈30% at 2 K, which rapidly decreases when approaching the transition temperature T_M, as shown in Figure 2b. Figure 2c shows the magnetic field dependence of the Hall resistance at different temperatures, in which the Hall resistance rapidly increases at lower temperatures. The nonlinear Hall behavior in the anomalous insulating state below T_M can be attributed to the two channels of the carrier, which might be related to the occupancy of different t_{2g} subbands of Ti ions.[38] With the fitting of these data, we extracted the temperature dependence of the carrier density and mobility, as summarized in Figure 2d. With decreasing temperature, the carrier density gradually decreases and then rapidly quenches (down to 10^{10} cm^{-2}) below T_M, while the mobility gradually increases and eventually saturates at ≈10^3 cm^2 V^{-1} s^{-1} in the insulating state, which is approximately three orders of magnitude larger than that at high temperatures (e.g., 200 K).

As argon-ion irradiation also introduces structural disorder at the sample surface as revealed by STEM analysis, we further investigated whether the disorder induced weak localization could account for the observed MIT as well as high electron mobility at low temperatures.[39,40] Disorder-induced weak localization can lead to a weak suppression of conductivity with decreasing temperature (T) in a 2D system, following a logarithmic relationship $\sigma(T) \sim \ln(T)$.[39,40] Clearly, the conductance of the TiO_2 surface decreases several orders of magnitude at low temperatures, and such a dramatic change cannot be scaled by the weak localization model with a logarithmic relationship (Figure S5, Supporting Information); instead, it can be nicely reproduced by an activation model with exponential term (Figure 2a).

The rapidly suppressed carrier density of the insulating state at low temperatures indicates the trapping of excess electrons, which further suggests the formation of localized states (e.g., polarons) at the irradiated TiO_2 surface. Polarons formed in titanate systems have been widely reported, such as in TiO_2 or n-type $BaTiO_3$.[2–4,41–43] Previous works suggested that electrons could be easily trapped at Ti sites or oxygen vacancies and that electron polarons were localized below the Fermi level of ≈0.4–1.3 eV.[42,43] The low activation energy (≈9 meV) of the insulating state at the irradiated TiO_2 surface implies the rather shallow nature of these localized states. We speculate that the difference between our results and the previous results might be related to the distinct oxygen vacancy concentrations. In our system, the Hall transport estimates the oxygen vacancy concentration in the range of ≈10^{13} to 10^{14} cm^{-2}, which is ≈1–2 orders of magnitude higher than that in previous studies.[42,43] Such a high carrier concentration confined at the surface might reduce the excitation energy between polaronic and free-carrier states through collective behavior. Interestingly to note that the rutile TiO_2 surfaces modified by nanometal clusters (e.g., Ag_5 or Cu_5) also exhibit a dual (localized vs delocalized) nature of polaronic states (convertible upon photoexcitation), in which the atomic clusters donate electrons into TiO_2 and enable the stabilization of multiple surface polarons.[44–47]

To further elaborate the nature of the coexistence of delocalized electrons and localized electron states, we performed in situ ionic liquid gating (ILG) on a metallic TiO_2 surface (inset of **Figure 3**a; Figure S6, Supporting Information), which has been widely used to tune the electron doping of materials through gate voltage (V_G).[30,48–51] Figure 3a shows the temperature dependence of the sheet resistance at different V_G. With increasing V_G, the sheet resistance at high temperature gradually decreases, which is due to the enhancement of the electron concentration. Interestingly, the sheet resistance changes only slightly with varying V_G when approaching the metal-to-insulator transition temperature, and more importantly the curves merge into the same trend below the T_M. As shown in Figure 3b, a further Arrhenius plot of the $R_{sheet}(T)$ curves shows a similar thermal activation energy of ≈9 meV for all gated states (inset of Figure 3b), coinciding with the feature of the shallow in-gap state formed below the conduction band. To gain further insight into the insulating state at low temperatures, we traced the evolution of the carrier density (i.e., electron doping level) with different V_G. As shown in Figure 3c,d, the magnetic field dependent Hall resistance measured at 200 K varies significantly with increasing V_G, while it remains almost unchanged at 10 K for different V_G. The extracted carrier density and mobility at different temperatures and V_G are summarized in Figure 3e,f. As V_G increases, the carrier density at high temperatures increases significantly. However, when approaching the MIT, the carrier density rapidly decreases, but follows a similar trend among different V_G.

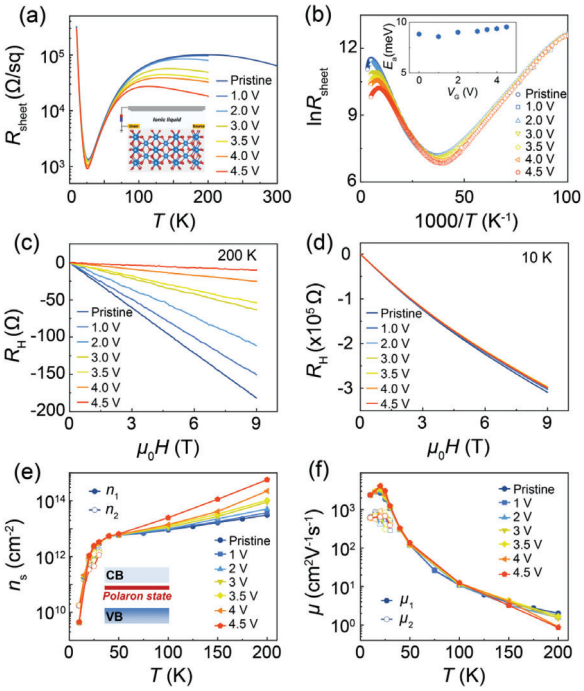

Figure 3. Ionic liquid gating induced electron doping on the rutile TiO_2 surface. a) Temperature dependence of sheet resistance at different gate voltages (V_G) through ionic liquid gating. The inset shows a schematic diagram of typical ionic liquid gating. b) Logarithmic sheet resistance as a function of reciprocal temperature at different V_G. The inset exhibits the activated energy E_a as a function of V_G. c,d) Magnetic field dependence of Hall resistance at different V_G for 200 K (c) and 10 K (d). e) Carrier density as a function of temperature at different V_G. The inset shows a sketch of the shallow polaron state forming in the gap. f) Mobility as a function of temperature at different V_G. The two carrier channels formed at low temperatures are denoted by filled and open dots.

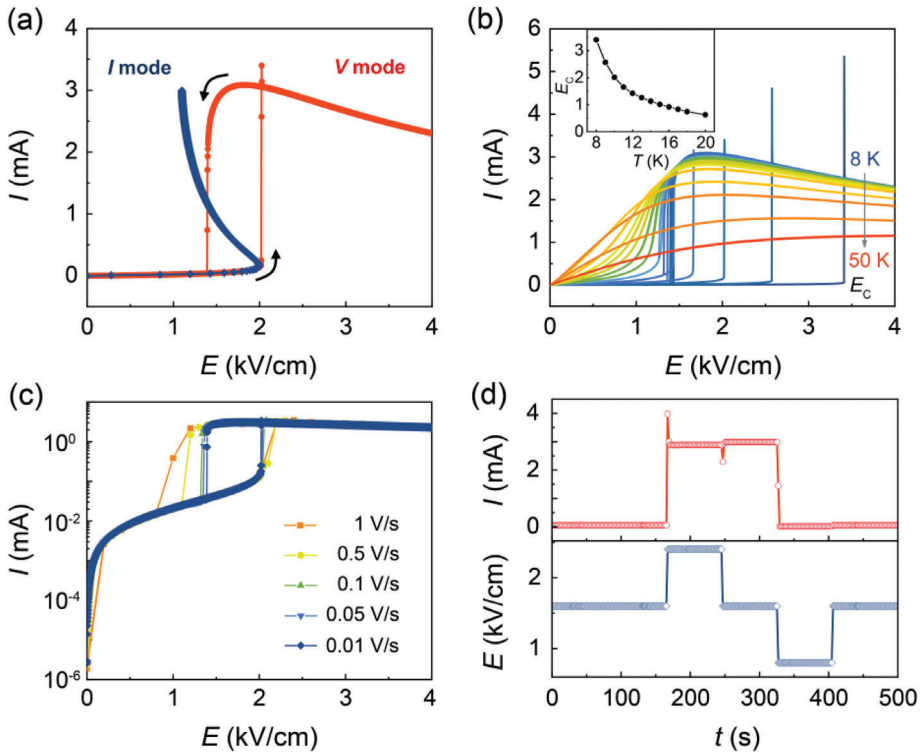

Figure 4. Electrically driven dissociation of localized electronic states. a) Measurements of current I vs electric field E (red) and E vs I (blue) modes for two terminal switches with 50 µm length and 20 µm width at 10 K. b) I–E curves at different temperatures. The inset shows the temperature dependence of the critical electric field E_C. c) I–E curves at different voltage sweeping rates. d) The variation in current I as the electric field E changes with time t.

These observations clearly demonstrate that such an insulating (localized) state at low temperatures is stable against electron doping, suggesting the formation of a robust ultrashallow localized in-gap state. With this, we could understand our exotic $R(T)$ curves based on the coexistence of high mobility electrons and localized electronic states. Specifically, with decreasing temperature, the majority of electrons in the 2DEG are localized at the Ti site or oxygen vacancies, which can be disassociated at high temperatures.[3,41,42] Consequently, the carrier density rapidly decreases as an MIT simultaneously occurs. At this stage, the remanent dilute electrons demonstrate a very high mobility, which could be attributed to the lower carrier concentration. The shallow-level polaronic state might be related to the 2D nature of 2DEG at the rutile TiO_2 surface.[13,52–57] Additionally, we noted that such an insulating state at low temperatures is a generic feature for different oriented rutile TiO_2 surfaces after argon-ion irradiation (Figure S7, Supporting Information), which indicates the TiO_2 surfaces form a unique and fertile playground to explore the 2DEG and localized electronic states as well their intriguing couplings.

2.3. Electrically Triggered Insulator-to-Metal Transition

Considering the small energy barrier between localized electronic states and delocalized electrons, one can naturally expect that an electric field might be able to change the barrier and hence dramatically release the localized electrons, leading to an insulator-to-metal transition (IMT). To testify this scenario, we applied a longitudinal electric field through the channel to activate the shallow in-gap state.[58] Herein, a two-terminal device was fabricated, and we monitored the changes of electrical current when changing the electric voltage. As shown in **Figure 4**a, the I–E curve at 10 K shows distinct hysteresis with sweeping voltage. A metallic state could be triggered once the electric field is above the critical electric field of E_C, which seems to slightly change with varying channel size (Figure S8, Supporting Information). We note that at low temperatures, the rutile TiO_2 surface is insulating at lower voltage, while it abruptly turns into a metallic state once it arrives at a critical value, which suggests the collapse of the in-gap state. In addition to the I–E mode, we also probed the sample with the E–I mode (blue curves in Figure 4a), and the absence of hysteresis indicates that the voltage, rather than current, induces an abrupt change. Furthermore, the hysteresis loop was gradually suppressed and eventually disappeared when approaching the MIT; accordingly, the critical electric field E_C required also decreased (Figure 4b). The hysteresis behavior of the I–E curve remains clear with different sweep rates of voltage ranging from 0.01 to 1 V/s (Figure 4c). The slight changes in the critical electric field E_C could be attributed to the capacitive effect by considering an insulating state at low temperatures.

We note that for electrically controlled IMT studies, Joule heating forms an inevitable effect during the application of an electric field.[59,60] We performed multiple switching cycles continuously at identical devices to determine whether Joule heating is dominant for the observed IMT, and the results demonstrate a rather robust and repeatable switching (Figure S9, Supporting Information). The cumulative probability plots among 100

cycled *I–E* curves (Figure S9b, Supporting Information) reveal that the current levels barely change through switching, suggesting the stability of the electric-field controlled switching. We note that if Joule heating is the dominant factor, the continuous cycles should be gradually changed due to the accumulation of heat. The time dependent current evolved with electric field shows robust and highly repeatable high and low current levels when the electric field reaches the curtain thresholds (Figure 4d; Figure S10, Supporting Information), which further endorses the intrinsic nature of this electric field induced IMT. To further quantify the impact of Joule heating on the measured IMT, we simulated the temperature distribution at the TiO_2 surface (Section S9, Supporting Information). Even with a threshold electric field applied across the metallic channel at 10 K (Figure S11, Supporting Information), the simulated temperature change at the channel is insignificant ($\Delta T \approx 1$ K). This further demonstrates that the electric field induces the IMT at low temperatures. Furthermore, if the Joule heating effect is dominant, the threshold input power (threshold voltage multiplied by the corresponding current) would decrease when approaching the transition temperature T_{MIT}, which contradicts our data (Figure S12, Supporting Information). Based on these points, we determined that the observed IMT is dominated by the electric field rather than Joule heating. At low temperatures, the electric field triggers the disassociation of localized states, resulting in an IMT.

3. Conclusion

We have shown the observation of a high-mobility 2DEG on the surface of rutile TiO_2 through ion-irradiation-induced chemical reduction and further observed an exotic MIT at lower temperature. Combining the ionic-liquid-gating-induced electron doping measurements, we further elaborated the coexistence and interconversion between delocalized- and localized-electrons. More importantly, we demonstrated that the insulating state formed by localized electrons can be activated to form highly conducting electrons through the application of an electric field. Our work sheds new light on the study of electronic states at the rutile TiO_2 surface, and provides a fertile playground to manipulate the coupling between localized electron state and conducting electron gas. The electric field tunable IMT offers a new strategy to design new resistive switching devices.

4. Experimental Section

Argon-Ion Irradiation: Commercially available rutile TiO_2 single crystals (5 mm × 5 mm × 0.5 mm, Hefei Kejing Material Technology Co., Ltd.) were used. The conducting surface was induced by argon-ion irradiation (AJA International, Inc.) by varying parameters (e.g., 200 V_30 s denotes beam voltage 200 V and dwell time 30 s), the beam voltage, acceleration voltage, and beam current were 200 V (300 V/400 V), 40 V (60 V/80 V), and 4 mA (12 mA/23 mA), respectively. The irradiation pressure was $\approx 2 \times 10^{-4}$ Torr at room temperature (the chamber background pressure was below 10^{-6} Torr). After irradiation, the samples were taken out in atmosphere and then transferred into either an ultrahigh vacuum chamber or a low-temperature refrigerator for XAS and electrical transport measurements, respectively.

Transport Measurement: For electrical measurements, the pristine sample was measured in a two-terminal configuration (Keithley Model 6517B High Resistance Meter) due to its large resistance, while the resistance of irradiated samples was measured by the van-der-Pauw method (PPMS) to remove the influence of contact resistance. For the in situ ILG study, a Hall bar geometry was used to measure magnetoresistance and Hall resistance. The insulator-to-metal switching behavior was studied using a two-terminal device (Keithley 2400). We mainly focused on the #300 eV_2 min sample. The Hall bar structure ($W/L \approx 0.6/2$ mm) was used for in situ ionic liquid gating, while two-terminal devices with different widths and lengths were applied for *I–V* curves. For device preparation, bare TiO_2 substrates with different masks were irradiated by argon ions, and then hall bar structures or two-terminal devices with a conducting region were obtained, followed by sputtered Ti/Au electrodes. For in situ ionic liquid gating, the device was placed in a quartz bowl covered entirely with IL, and a slice of Pt was used as the gate electrode. For each V_G, the measured conditions were the same. The V_G was changed at room temperature with a dwell time of 10 min for each cycle. All transport measurements were performed in a physical property measurement system (PPMS, 9 T, Quantum Design).

Scanning Transmission Electron Microscopy: The irradiated rutile (001) TiO_2 surface was covered by Au, and then cross-sectional samples were prepared using a focused ion beam (FIB) instrument. The images were acquired on a probe corrected STEM (FEI Titan Cubed Themis 60–300) operated at 300 kV. The collection angle range of the detector was 64–200 mrad.

X-ray Absorption Spectroscopy: XAS measurements at titanium *L*-edges and oxygen *K*-edges were performed at beamline 08U1A of Shanghai Synchrotron Radiation Facility, and beamlines 4.0.2 and 6.3.1 of Advanced Light Source. The XAS spectra were obtained at room temperature through the total electron yield (TEY) mode with signals normalized to the photon flux measured by the photocurrent of a clean gold mesh.

Supporting Information

Supporting Information is available from the Wiley Online Library or from the author.

Acknowledgements

S.S. and M.W. contributed equally to this work. This study was financially supported by the National Basic Research Program of China (grant Nos. 2021YFE0107900 and 2021YFA1400300); the Beijing Nature Science Foundation (grant No. Z200007); the Basic Science Center Project of NFSC (grant No. 52388201); the National Key Research and Development Program of China (grant No. 2022YFB3807602); the National Natural Science Foundation of China (grant Nos. 52025024, 51872155 and 52250281); and the State Key Laboratory of New Ceramic and Fine Processing Tsinghua University (No. KF202201). This work made use of the resources of the National Center for Electron Microscopy in Beijing.

Conflict of Interest

The authors declare no competing financial interest.

Data Availability Statement

The data that support the findings of this study are available from the corresponding author upon reasonable request.

Keywords

2D electron gas, polarons, rutile titanium dioxides, surfaces

Received: February 14, 2023
Revised: April 18, 2023
Published online: June 11, 2023

[1] I. G. Austin, N. F. Mott, *Adv. Phys.* **2001**, *50*, 757.
[2] M. Reticcioli, U. Diebold, G. Kresse, C. Franchini, in *Handbook of Materials Modeling: Applications: Current Emerging Materials*, Springer International Publishing, Cham, Switzerland **2020**.
[3] C. Franchini, M. Reticcioli, M. Setvin, U. Diebold, *Nat. Rev. Mater.* **2021**, *6*, 560.
[4] J. R. De Lile, A. Bahadoran, S. Zhou, J. Zhang, *Adv. Theory Simul.* **2022**, *5*, 2100244.
[5] A. S. Alexandrov, *Polarons in Advanced Materials*, *103*, Springer Science & Business Media, Berlin, Germany **2008**.
[6] Y. Li, Y. Zhu, M. Wang, M. Zhao, J. Xue, J. Chen, T. Wu, S. A. Chambers, *Adv. Funct. Mater.* **2022**, *32*, 2203491.
[7] E. K. H. Salje, A. S. Alexandrov, W. Y. Liang, *Polarons and Bipolarons in High-T_c Superconductors and Related Materials*, Cambridge University Press, Cambridge, UK **2009**.
[8] H. M. Rønnow, C. Renner, G. Aeppli, T. Kimura, Y. Tokura, *Nature* **2006**, *440*, 1025.
[9] M. Wang, C. Bi, L. Li, S. Long, Q. Liu, H. Lv, N. Lu, P. Sun, M. Liu, *Nat. Commun.* **2014**, *5*, 4598.
[10] M. Reticcioli, M. Setvin, X. F. Hao, P. Flauger, G. Kresse, M. Schmid, U. Diebold, C. Franchini, *Phys. Rev. X* **2017**, *7*, 031053.
[11] C. Verdi, F. Caruso, F. Giustino, *Nat. Commun.* **2017**, *8*, 15769.
[12] L. Sun, X. M. Hao, Q. L. Meng, L. G. Wang, F. Liu, M. Zhou, *Adv. Electron. Mater.* **2019**, *5*, 1900271.
[13] T. Sarkar, K. Gopinadhan, J. Zhou, S. Saha, J. M. D. Coey, Y. P. Feng, Ariando, T. Venkatesan, *ACS Appl. Mater. Interfaces* **2015**, *7*, 24616.
[14] S. X. Zhang, D. C. Kundaliya, W. Yu, S. Dhar, S. Y. Young, L. G. Salamanca-Riba, S. B. Ogale, R. D. Vispute, T. Venkatesan, *J. Appl. Phys.* **2007**, *102*, 013701.
[15] J. Li, S. Chenot, J. Jupille, R. Lazzari, *Phys. Rev. B* **2020**, *102*, 081401.
[16] Y. Mao, X. Ma, D. Wu, C. Lin, H. Shan, X. Wu, J. Zhao, A. Zhao, B. Wang, *Nano Lett.* **2020**, *20*, 8067.
[17] W. Kong, J. Zhou, Y. Z. Luo, T. Yang, S. Wang, J. Chen, A. Rusydi, Y. P. Feng, M. Yang, *Phys. Rev. B* **2019**, *100*, 085413.
[18] M. Reticcioli, Z. Wang, M. Schmid, D. Wrana, L. A. Boatner, U. Diebold, M. Setvin, C. Franchini, *Nat. Commun.* **2022**, *13*, 4311.
[19] E. Yagi, R. R. Hasiguti, M. Aono, *Phys. Rev. B* **1996**, *54*, 7945.
[20] Y. Xing, H.-M. Zhang, H.-L. Fu, H. Liu, Y. Sun, J.-P. Peng, F. Wang, X. Lin, X.-C. Ma, Q.-K. Xue, J. Wang, X. C. Xie, *Science* **2015**, *350*, 542.
[21] C. Spreafico, J. VandeVondele, *Phys. Chem. Chem. Phys.* **2014**, *16*, 26144.
[22] A. Janotti, C. Franchini, J. B. Varley, G. Kresse, C. G. Van de Walle, *Phys. Status Solidi RRL* **2013**, *7*, 199.
[23] L. Yan, J. E. Elenewski, W. Jiang, H. Chen, *Phys. Chem. Chem. Phys.* **2015**, *17*, 29949.
[24] L. Zhao, B. Magyari-Köpe, Y. Nishi, *Phys. Rev. B* **2017**, *95*, 054104.
[25] C. Guo, X. Meng, H. Fu, Q. Wang, H. Wang, Y. Tian, J. Peng, R. Ma, Y. Weng, S. Meng, E. Wang, Y. Jiang, *Phys. Rev. Lett.* **2020**, *124*, 206801.
[26] C. Cheng, Y. Zhu, W. H. Fang, R. Long, O. V. Prezhdo, *JACS Au.* **2022**, *2*, 234.
[27] Z. Zhang, H. Yan, J. Shen, S. Wang, K. Jin, *Scr. Mater.* **2022**, *216*, 114741.
[28] I. Lazić, E. G. T. Bosch, S. Lazar, *Ultramicroscopy* **2016**, *160*, 265.
[29] Y. Hwu, Y. D. Yao, N. F. Cheng, C. Y. Tung, H. M. Lin, *Nanostruct. Mater.* **1997**, *9*, 355.
[30] T. C. Rossi, D. Grolimund, O. Cannelli, G. F. Mancini, C. Bacellar, D. Kinschel, J. R. Rouxel, N. Ohannessian, D. Pergolesi, M. Chergui, *J. Synchrotron Radiat.* **2020**, *27*, 425.
[31] F. M. F. de Groot, J. Faber, J. J. M. Michiels, M. T. Czyżyk, M. Abbate, J. C. Fuggle, *Phys. Rev. B* **1993**, *48*, 2074.
[32] P. A. van Aken, B. Liebscher, V. J. Styrsa, *Phys. Chem. Miner.* **1998**, *25*, 494.
[33] C. M. Yim, M. B. Watkins, M. J. Wolf, C. L. Pang, K. Hermansson, G. Thornton, *Phys. Rev. Lett.* **2016**, *117*, 116402.
[34] M. Reticcioli, M. Setvin, X. Hao, P. Flauger, G. Kresse, M. Schmid, U. Diebold, C. Franchini, *Phys. Rev. X* **2017**, *7*, 031053.
[35] O. Hiroshi, F. Ken-ichi, I. Yasuhiro, *Bull. Chem. Soc. Jpn.* **1995**, *68*, 2447.
[36] L. Mohrhusen, J. Kräuter, M. Willms, K. Al-Shamery, *J. Phys. Chem. C* **2019**, *123*, 20434.
[37] P. He, S. M. Walker, S. S. L. Zhang, F. Y. Bruno, M. S. Bahramy, J. M. Lee, R. Ramaswamy, K. Cai, O. Heinonen, G. Vignale, F. Baumberger, H. Yang, *Phys. Rev. Lett.* **2018**, *120*, 266802.
[38] J. Biscaras, N. Bergeal, S. Hurand, C. Grossetête, A. Rastogi, R. C. Budhani, D. LeBoeuf, C. Proust, J. Lesueur, *Phys. Rev. Lett.* **2012**, *108*, 247004.
[39] B. L. Altshuler, D. Khmel'nitzkii, A. I. Larkin, P. A. Lee, *Phys. Rev. B* **1980**, *22*, 5142.
[40] P. A. Lee, T. V. Ramakrishnan, *Rev. Mod. Phys.* **1985**, *57*, 287.
[41] H. Ihrig, *J. Phys. C: Solid State Phys.* **1976**, *9*, 3469.
[42] P. Deák, B. Aradi, T. Frauenheim, *Phys. Rev. B* **2012**, *86*, 195206.
[43] M. Setvin, C. Franchini, X. Hao, M. Schmid, A. Janotti, M. Kaltak, C. G. Van de Walle, G. Kresse, U. Diebold, *Phys. Rev. Lett.* **2014**, *113*, 086402.
[44] M. P. de Lara-Castells, A. W. Hauser, J. M. Ramallo-López, D. Buceta, L. J. Giovanetti, M. A. López-Quintela, F. G. Requejo, *J. Mater. Chem. A* **2019**, *7*, 7489.
[45] P. López-Caballero, S. Miret-Artés, A. O. Mitrushchenkov, M. P. de Lara-Castells, *J. Chem. Phys.* **2020**, *153*, 164702.
[46] P. López-Caballero, J. M. Ramallo-López, L. J. Giovanetti, D. Buceta, S. Miret-Artés, M. A. López-Quintela, F. G. Requejo, M. P. de Lara-Castells, *J. Mater. Chem. A* **2020**, *8*, 6842.
[47] M. P. de Lara-Castells, S. Miret-Artés, *Europhys. News* **2022**, *53*, 7.
[48] C. Leighton, *Nat. Mater.* **2019**, *18*, 13.
[49] N. Lu, P. Zhang, Q. Zhang, R. Qiao, Q. He, H. B. Li, Y. Wang, J. Guo, D. Zhang, Z. Duan, Z. Li, M. Wang, S. Yang, M. Yan, E. Arenholz, S. Zhou, W. Yang, L. Gu, C. W. Nan, J. Wu, Y. Tokura, P. Yu, *Nature* **2017**, *546*, 124.
[50] A. M. Goldman, *Annu. Rev. Mater. Res.* **2014**, *44*, 45.
[51] S. Shen, Z. Li, Z. Tian, W. Luo, S. Okamoto, P. Yu, *Phys. Rev. X* **2021**, *11*, 021018.
[52] K. P. McKenna, M. J. Wolf, A. L. Shluger, S. Lany, A. Zunger, *Phys. Rev. Lett.* **2012**, *108*, 116403.
[53] D. G. Ouellette, P. Moetakef, T. A. Cain, J. Y. Zhang, S. Stemmer, D. Emin, S. J. Allen, *Sci. Rep.* **2013**, *3*, 3284.
[54] M. Kang, S. W. Jung, W. J. Shin, Y. Sohn, S. H. Ryu, T. K. Kim, M. Hoesch, K. S. Kim, *Nat. Mater.* **2018**, *17*, 676.
[55] J. Jeong, N. Aetukuri, T. Graf, T. D. Schladt, M. G. Samant, S. S. P. Parkin, *Science* **2013**, *339*, 1402.
[56] V. V. Kabanov, O. Y. Mashtakov, *Phys. Rev. B* **1993**, *47*, 6060.
[57] W. J. Yin, B. Wen, C. Y. Zhou, A. Selloni, L. M. Liu, *Surf. Sci. Rep.* **2018**, *73*, 58.
[58] L. Zhu, J. Zhou, Z. Sun, *Mater. Res. Lett.* **2018**, *6*, 165.
[59] J. del Valle, P. Salev, F. Tesler, N. M. Vargas, Y. Kalcheim, P. Wang, J. Trastoy, M.-H. Lee, G. Kassabian, J. G. Ramírez, M. J. Rozenberg, I. K. Schuller, *Nature* **2019**, *569*, 388.
[60] Y. Kalcheim, A. Camjayi, J. del Valle, P. Salev, M. Rozenberg, I. K. Schuller, *Nat. Commun.* **2020**, *11*, 2985.